Accepted Manuscript

Structural, electrical, optical and magnetic properties of SmCrO$_3$ chromites: Influence of Gd and Mn co-doping

Neeraj Panwar, Indrani Coondoo, Surendra Kumar, Sandeep Kumar, M. Vasundhara, Ashok Rao

Structural, Electrical, Optical and Magnetic Properties of SmCrO$_3$ chromites: Influence of Gd and Mn co-doping

Neeraj Panwar[1, a], Indrani Coondoo[2], Surendra Kumar[1], Sandeep Kumar[1], M. Vasundhara[3], Ashok Rao[4, b]

[1]Department of Physics, Central University of Rajasthan Bandarsindri, Ajmer-305817, Rajasthan, India

[2]Department of Physics & CICECO- Aveiro Institute of Materials, University of Aveiro, 3810-193 Aveiro, Portugal

[3]Materials Science and Technology Division, CSIR-National Institute for Interdisciplinary Science and Technology, Industrial Estate, Trivandrum 695 019, India

[4]Department of Physics, Manipal Institute of Technology, Manipal Academy of Higher Education, Manipal 576104, Karnataka, India

Impact of co-doping of Gadolinium (Gd) and Manganese (Mn) ions on the structural, electrical, optical and magnetic properties of SmCrO$_3$ (SCO) orthochromite compound has been systematically investigated for the first time. The lattice volume expanded with only Mn substitution whereas it shrinks in the co-doped compounds. The tolerance factor decreased while the orthorhombic distortion was found to increase with co-doping. Tilt angle, $\theta_{[101]}$ ($^{\text{o}}$) increased in the co-doped compounds. On the contrary, $\emptyset_{[010]}$ ($^{\text{o}}$) initially decreased and then increased. The increased orthorhombic distortion with co-doping also influenced the Raman modes. The electrical resistivity got enhanced in the co-doped samples and its behavior was explained based

on Mott's variable range hopping model. Hopping energy and mean hopping distance have also been estimated for the co-doped compounds. The optical bandgap of pristine SCO compound was observed to vary with co-doping, signifying the potential applications of these compounds as photocatalyst. Two compensation temperatures (defined as a temperature where the magnetization changes polarity) were noticed in co-doped compounds. The magnetization reversal was observed in all the co-doped compounds under lower applied magnetic field. The low temperature magnetocaloric effect got enhanced significantly with increasing co-doping content implying the usefulness of these compounds as low temperature refrigerant materials.

Keywords: Orthochromites; electrical-; optical-; magnetic- properties

---

[a] Corresponding author's email: neerajpanwar@curaj.ac.in

[b] Co-corresponding author's email: a.rao@manipal.edu

1. Introduction

Multiferroics, with more than one ferroic order, are one of the most important class of materials being investigated widely due to the presence of strong correlations between their structural, magnetic and electric properties [1-2]. Orthochromites, with the general chemical formula RCrO$_3$ (R = Y or trivalent rare-earth ion) and a distorted orthorhombic structure, belong to the family of multiferroics. Due to the competition of magnetic exchange interactions between Cr^{3+} and R^{3+} ions, they exhibit very exciting phenomena such as: field and temperature induced magnetization reversal (TIMR), spin reorientation (SR) and exchange bias (EB) [3-11]. These properties are useful in magnetic data storage, thermally assisted magnetic read heads, thermo-magnetic switches, and thermally assisted magnetic random access memories [8, 12-15]. Moreover, they demonstrate canted antiferromagnetism (CAFM) in G-type configuration below the Néel temperature (T_N) in the range of 110 - 290 K, which depends upon the ionic size of the tri-valent rare-earth ion(s) present [3-5, 9, 16]. The canted AFM arises due to the antisymmetric Dzyaloshinskii-Moriya (DM) interaction and is responsible for the appearance of weak ferromagnetism in these materials [17-18]. The semiconducting nature of orthochromites may also play a significant role in the future ultra-violet photonic and spin-photonic devices such as solid-oxide fuel cells, magneto-optical properties, catalytic converters, solar blind UV photodetectors, light-emitting diodes and gas sensors etc. [19-25].

Orthochromites are also useful in low temperature magnetic refrigeration [5, 26-28]. The research towards the development of a new magnetic refrigeration technology has increased in the last two decades. This technology is based on magnetocaloric effect (MCE). It has an attractive perspective related to materials utilization as cheaper, safer, more efficient, and environment friendly in comparison to the standard gas-based cooling techniques. The magnetic

entropy change (ΔS) and the relative cooling power (RCP) parameters decide the MCE. For example, Yin *et al.* observed giant MCE at 2 K in GdCrO$_3$ single crystal due to the ordering of Gd^{3+} ions. The value of $-\Delta S$ was equal to 31.6 J/kg K for a field change (ΔH) of 44 kOe [29]. In another rare-earth compound, HoCrO$_3$, a value of $-\Delta S$ = 4.2 J/kg K at 20 K for a ΔH of 40 kOe has been reported. It was observed that by Gd doping at Ho-site, MCE can further be enhanced, and the value of $-\Delta S$ ~ 8.5 J/kg K was observed in Ho$_{0.67}$Gd$_{0.33}$CrO$_3$ under the same (ΔH, T) conditions [26]. McDannald *et al.* demonstrated $-\Delta S$ = 4.6 J/kg K and RCP = 217 J/kg for the DyCrO$_3$ system in 5 - 30 K temperature range at 40 kOe of ΔH magnetic field variation [30].

Among all the chromite compounds, SmCrO$_3$ (SCO) has gained significant attention recently. It depicts paramagnetic to canted AFM transition ~192 K due to the ordering of Cr^{3+} spins. Further, with lowering temperature, the spontaneous change in magnetic structure, known as spin reorientation transition, occurs ~ 34 K due to the rotation of Cr^{3+} spins from one easy direction to the other [31-32]. The controversy of magnetization reversal in SCO is yet to settle down. For example, Gupta *et al.* reported giant temperature dependent magnetization reversal along with a large exchange bias and coercivity in SCO compound [31]. The magnetization reversal occurred due to the internal field generated by the canted Cr^{3+} spins on the rare-earth site. This internal field causes the rotation of Sm^{3+} spins opposite to the canted Cr^{3+} AFM component. On the contrary, Wu *et al.* and Dash *et al.* could not detect any signature of magnetization reversal in this compound [32-33]. Dielectric studies on SCO compound showed colossal dielectric constant on the order of ~ 10^4 at room temperature which was associated to the grain boundary effects [34]. SCO also exhibits signature of ferroelectricity confirmed through dielectric and Raman spectroscopic techniques [34-35]. These properties make SCO a multiferroic material. As far as its magnetocaloric properties are concerned, Gupta and Poddar

4

observed inverse and direct magnetic entropy change at and above spin reorientation transition (T_{SR}) with $-\Delta S_{max}$ values $\sim -24\times10^{-2}$ & 13×10^{-2} J/kg-K, respectively [36]. Kumar *et al.* induced magnetization reversal in SCO compound with manganese substitution at chromium sites and observed an enhancement in MCE at low temperatures in comparison to the pristine one [6]. Recently, we have studied $Sm_{0.9}Gd_{0.1}Cr_{0.85}Mn_{0.15}O_3$ compound and reported magnetization reversal and the enhanced MCE [37].

In this article, we have investigated structural, optical, electrical properties of the $SmCrO_3$ and $Sm_{1-x}Gd_xCr_{0.85}Mn_{0.15}O_3$ ('x' = 0, 0.10, 0.20 and 0.50) orthochromites. Additionally, the magnetic and magnetocaloric properties of co-doped compounds have also been explored. Such studies have been scarcely carried out in co-doped orthochromite compounds. Therefore, through this work we report them in $Sm_{1-x}Gd_xCr_{0.85}Mn_{0.15}O_3$ orthochromites.

2. Experimental details

$SmCrO_3$ and $Sm_{1-x}Gd_xCr_{0.85}Mn_{0.15}O_3$ (with 'x' = 0, 0.10, 0.20 and 0.50) compounds were prepared by solid-state reaction method using high purity Sm_2O_3 (99.9%), Gd_2O_3 (99.99%), Cr_2O_3 (99.9%) and MnO_2 (99.99%) as starting materials. Details of the samples synthesis procedure and x-ray diffraction measurements are given in ref. [37]. In this article, we have coined the abbreviations as SCO, SCMO, 10SGCMO, 20SGCMO and 50SGCMO for $SmCrO_3$, $SmCr_{0.85}Mn_{0.15}O_3$, $Sm_{0.9}Gd0_{.1}Cr_{0.85}Mn_{0.15}O_3$, $Sm_{0.8}Gd_{0.2}Cr_{0.85}Mn_{0.15}O_3$ and $Sm_{0.5}Gd_{0.5}Cr_{0.85}Mn_{0.15}O_3$ compounds, respectively and henceforth only these abbreviations will be used. The field emission scanning electron microscopy (FESEM) images were acquired using a Mira3 TESCAN instrument. Raman spectra were recorded at room temperature in the frequency range 100 - 800 cm^{-1} using a Raman spectrometer (Thermo fisher scientific) with an excitation source of 532 nm wavelength. Temperature dependent electrical resistivity $\rho(T)$

measurements were performed using standard four-probe technique in the temperature range of 220 - 310 K. Optical absorbance measurement of the samples was carried out at room temperature using the Perkin Elmer Lambda 750 UV - Vis - NIR spectrophotometer in the wavelength range of 300 - 1000 nm. Magnetization was measured using a vibrating sample magnetometer attached to a physical property measurement system (Quantum Design Inc., USA).

3. Result and discussion

3.1 Structural and morphology study

Fig. 1 (a-c) displays the XRD patterns of few compounds viz. SCO, 20SCMO and 50SGCMO along with Rietveld refinement using *Fullprof* software. The best refinement was completed by choosing *Pnma* space group with orthorhombic structure. The lattice parameters of all the compounds were calculated from the refinement and summarized in table 1. The lattice parameters of the SCO and SCMO samples are found to be comparable to the reported data [6, 37]. It is noticed that the lattice volume of the SCMO compound is larger than that of SCO. This is attributed to the larger size of Mn^{3+} ion (r_{Mn}^{3+} = 0.645 Å) when compared with Cr^{3+} ion (r_{Cr}^{3+} = 0.615 Å). As we substitute Gd^{3+} ions at Sm-site, the lattice volume decreases with the increasing Gd substitution, owing to the smaller ionic radius of Gd^{3+} ion (r_{Gd}^{3+} = 1.053 Å) in comparison to Sm^{3+} ion (r_{Sm}^{3+} = 1.079 Å) [38]. The average rare-earth ionic radius $R_{avg.} = \sqrt{(X_{Gd} \times R_{Gd}^2) + ((1-x)_{Sm} \times R_{Sm}^2)}$ of the compounds is tabulated in table 1. The Goldschmidt tolerance factor (t) has a great role in deciding the stability of the perovskite structure. We have calculated the tolerance factor for all the compounds (summarized in table 1) using the formula, $t = (R_A + R_O)/\sqrt{2}(R_B + R_O)$; where R_A and R_B are the average ionic radii of rare-earth and

6

chromium site cations, and R_O is the ionic radius of anion (O^{2-}). These values are in accordance with the proposed range of 't' in between, $0.75 < t < 0.9$, for an orthorhombic distorted structure [39 - 40]. The orthorhombic distortion of the unit cell from the ideal cubic structure, defined by the orthorhombic strain factor $S = 2(a - c)/(a + c)$, was calculated and shown in table 1. From there, it can be noticed that 't' decreases but 'S' increases with decreasing $R_{avg.}$ Further, to quantify the octahedral distortion, the octahedral bond length $(B - O)$ and tilt angles were calculated from the lattice parameters according to the Zhao formalism [41]; $B - O = ab/4c$, $\theta_{[101]} = \cos^{-1}(c/a)$ and $\emptyset_{[010]} = \cos^{-1}(\sqrt{2}c/b)$ [table 1]. It can be seen that $B - O$ bond length increases in the co-doped samples because of larger ionic size of Mn^{3+} ions than Cr^{3+} ions. The tilt angles of the SCO compound are found to be comparable to the reported data [40]. The BO_6 octahedron rotates around both planes i.e. in-plane (along a and c axis) and out-of-plane (along b axis). The in-plane tilt $\theta_{[101]}$ is more than the out-of-plane tilt $\emptyset_{[010]}$ [table 1]. Here, one can notice that with only Mn doping i.e. in SCMO compound, $\theta_{[101]}$ value increases whereas $\emptyset_{[010]}$ decreases with respect to the pristine compound. Effect of Gd doping is opposite as the values for both the angles increase with increasing Gd content indicating an increase in the orthorhombic distortion. The $\emptyset_{[101]}$ value in the 50SGCMO is near to undoped SCO compound because with increasing Gd content two rotations occur about the $\emptyset_{[010]}$ axes and with increasing the doping concentration of Gd ions the rotation angles cancel each other (please refer to 3D crystal cell structure for SCO, 20SGCMO, and 50SGCMO compounds in Fig. 1).
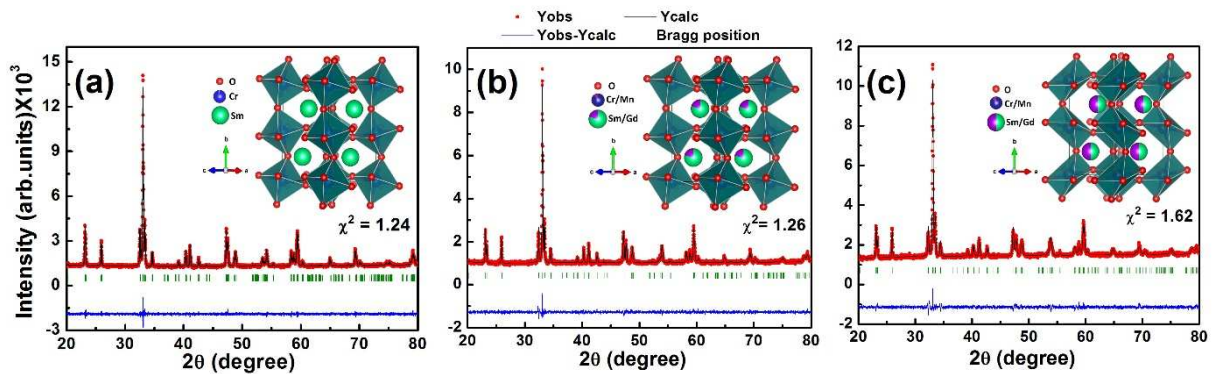
7

Figure 1: (**a-c**) Rietveld analysis results of the powder XRD patterns along with the 3D crystal cell structure for SCO, 20SGCMO, and 50SGCMO compounds.

Table 1: Lattice parameters, tolerance factor (*t*), orthorhombic strain (*S*), average A-site ionic radius (R_{avg}), bond length (<B-O>), octahedral tilt angles, crystallite size and average grain size (*G*) of the compounds.

Samples	SCO	SCMO	10SGCMO	20SGCMO	50SGCMO
a (Å)	5.5013(2)	5.5176(1)	5.5203(2)	5.5250(3)	5.5411(2)
b (Å)	7.6451(2)	7.6345(3)	7.6292(3)	7.6257(1)	7.6138(1)
c (Å)	5.3676(1)	5.3689(2)	5.3631(2)	5.3589(1)	5.3437(2)
V (Å^3)	225.7504	226.1601	225.8694	225.7811	225.4444
t	0.871	0.869	0.868	0.867	0.865
S	0.0246	0.0273	0.0288	0.0305	0.0362
R_{avg} (Å)	1.079	1.079	1.076	1.073	1.066
<B-O> (Å)	1.9588	1.9614	1.9632	1.9655	1.9737
$\theta_{[101]}$ (^{o})	12.66	13.35	13.69	14.09	15.34
$\emptyset_{[010]}$ (^{o})	6.81	6.02	6.17	6.37	6.99
Crystallite size (nm)	94.78	87.56	119.05	166.11	219.29
G (μm)	0.73	1.34	1.41	1.51	2.19

The Raman spectroscopy is a useful technique to investigate the local structure change of a material as a result of doping. The orthorhombic space group *Pnma* ($a^- b^+ a^-$ in Glazer's

8

notation) [42], results from the distortion of an ideal cubic $Pm\bar{3}m$ perovskite structure. There are three types of distortions in CrO_6 octahedron including tilt, octahedron rotation, and R-cation displacement. The cubic symmetry is broken due to these distortions. According to group theory, 24 Raman-active modes belong to the following irreducible representation [43]: $\left(\Gamma = 7A_g + 5B_{1g} + 8B_{1u} + 7B_{2g} + 5B_{3g}\right)$ in $Pnma$ structure. Here, we identified 11 Raman active modes in SCO sample at room temperature as shown in Fig. 2 (a). The other modes of the RCrO$_3$ system, being too weak in intensity or have energies below the experimental cut-off, are obscured. The rare-earth ions being heavier than the transition metal ions will cause the bonds to vibrate at lower wave numbers. Therefore, A_g (2) and B_{2g} (1) modes result from the rare-earth ion vibrations. Moreover, these modes shift to lower wavenumber side on Gd substitution because of the heavier mass of Gd^{3+} ion than Sm^{3+} ion. A_g (4) singlet is associated to Sm-O vibration. This mode gets broader and becomes diffused in co-doped compounds owing to the increase in disorder at the rare-earth site. The A_g (5), B_{1g} (2) and A_g (6) modes, corresponding to the bending of O-Cr-O bonds inside the octahedron, get distorted with co-doping due to the change in tilt angles. The wavenumber related to the A_g (6) mode follows the trend of $\emptyset_{[010]}$ angle (table 1) as its value decreases with Mn doping and thereafter its value increases with increase in Gd content (dashed line in Fig. 2). The phonon hardening (blue shift) of B_{3g} (1) mode indicated the possible displacement of rare-earth ions induced by spin-phonon coupling that results from the rare-earth and Cr^{3+}/Mn^{3+} ions interactions. The B_{3g} modes above 500 cm^{-1} are assigned to the antisymmetric stretching of O$_1$ and O$_2$ atoms in CrO_6 octahedron [28, 44] and are related to tilt angle $\theta_{[101]}$. The mixing of B_{3g} (4) and B_{2g} (4) modes is observed along with an increase in the intensity of the peak around ~ 673 cm^{-1}, ~ 672 cm^{-1}, ~ 670 cm^{-1} and ~ 661 cm^{-1} for SCMO, 10SGCMO, 20SGCMO and 50SGCMO compounds in comparison to pure SCO sample. This is

9

related an increase in the value of $\theta_{[101]}$ tilt angle with doping as can be seen from table 1. Thus,
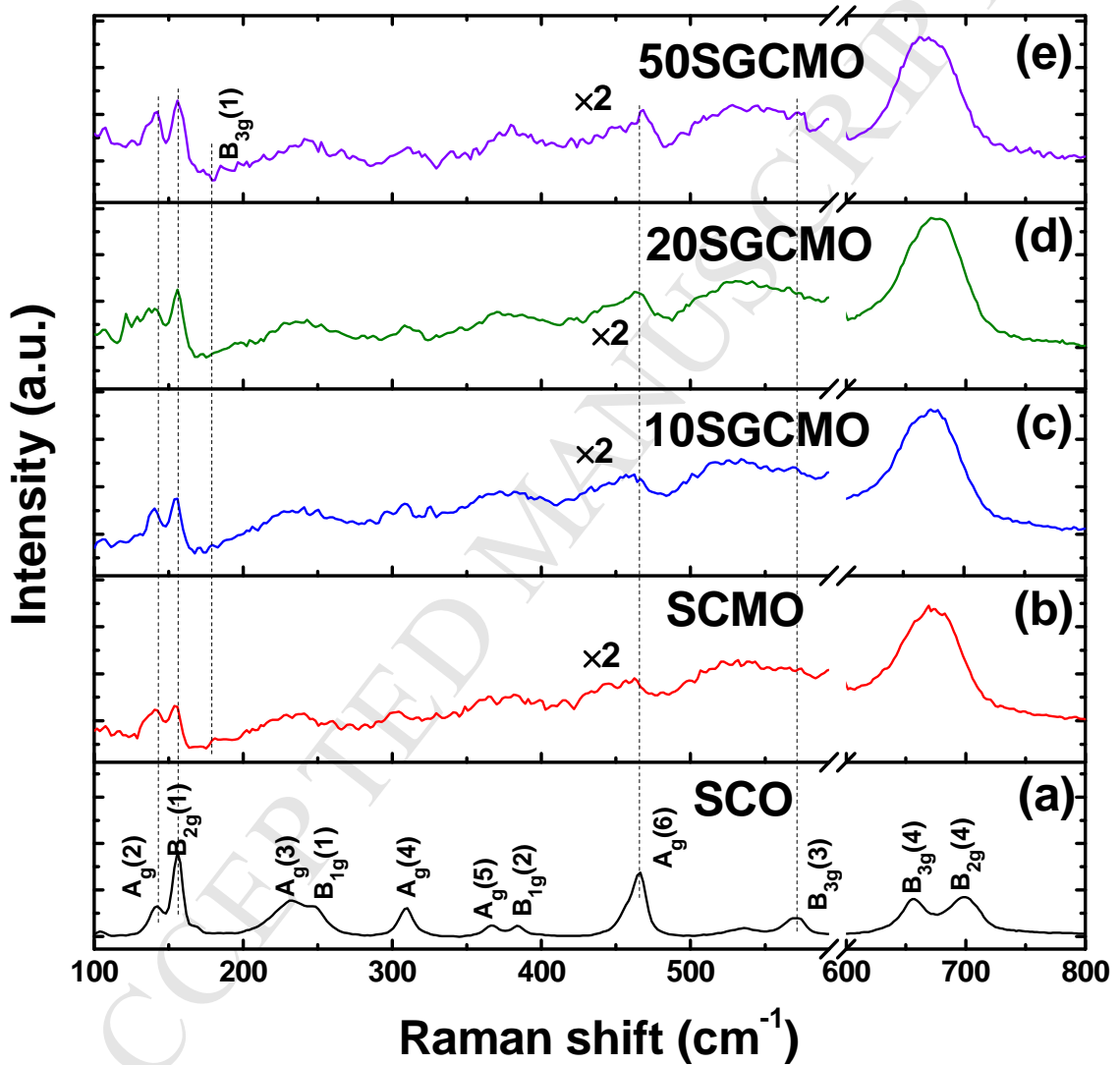
Raman results are consistent with the XRD analysis.

Figure 2: Room temperature Raman spectra of (a) SCO, (b) SCMO, (c) 10SGCMO, (d) 20SGCMO and 50SGCMO compounds. The horizontal axis shows a break from 593 to 600 cm^{-1}, because the B_{2g} (4) and B_{3g} (4) modes are much stronger than other modes in case of (b), (c),

(d) and (e). The curves in the range of 100 - 593 cm^{-1} were amplified by two times for clarity. Vertical dashed lines are guide to the eyes.

The FESEM images illuminating the surface morphology of SCO, SCMO, and 20SGCMO compounds are shown in Fig. 3 (a-c). The grain growth takes place during the sintering process and micrographs reveal the polyhedral shape grains of varying size. The average grain size (*G*) of all the compounds was estimated with the help of Microsoft Visio-2013 software. The grain size distribution histograms are shown in Fig. 3 (right side). The average grain size increased from SCO to 50SGCMO (listed in table1). The growth in orthorhombic distortion with increasing Gd-content may lead to the development of the stress and mass will flow. This will result in the observed grain growth in the co-doped compounds. Table 1 also depicts the values of crystallite size obtained from the modified Debye-Scherrer formulation (i.e. Williamson - Hall relation). It can be noticed for the co-doped compounds that the average grain size and the crystallite size follow the similar trend, however, the former shows larger value than the latter because an average grain consists of several crystallites.
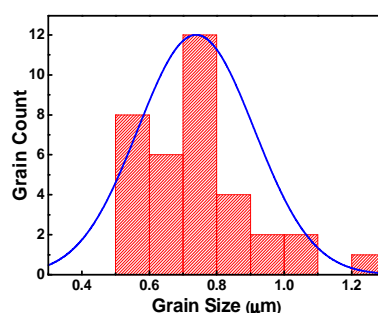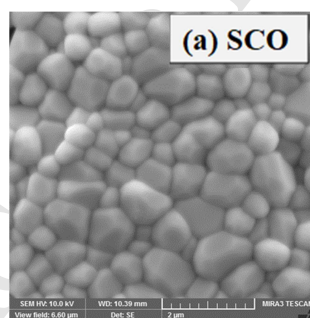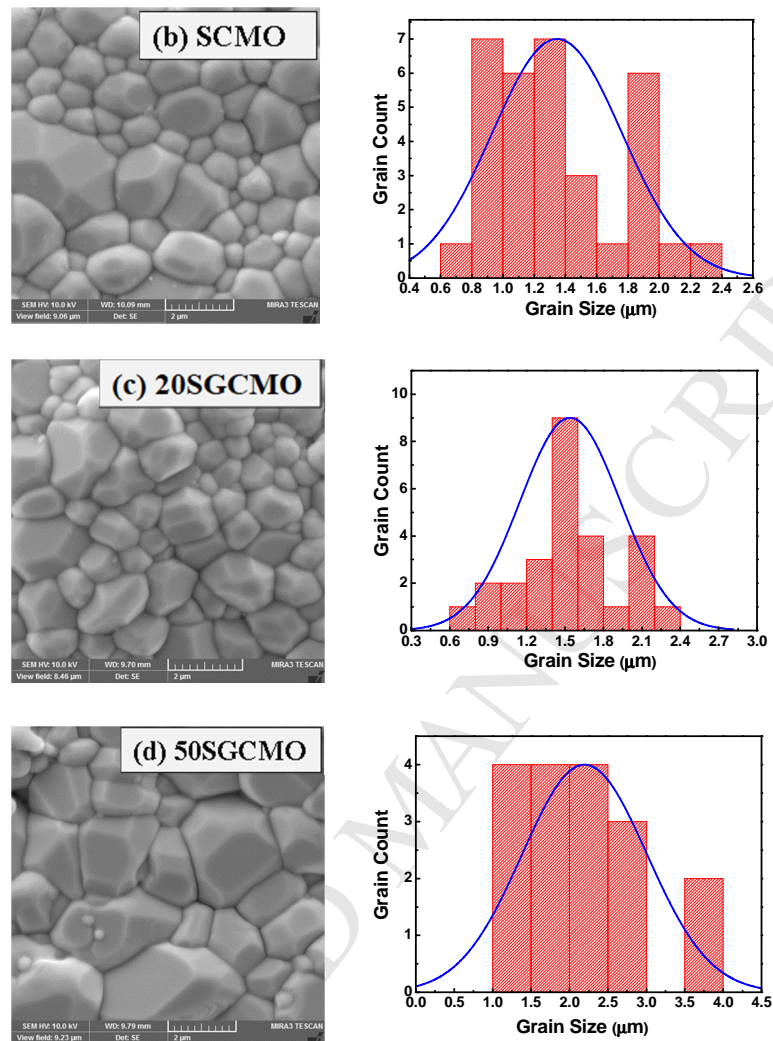
Figure 3: (**a-d**) FESEM images of the sintered pellets, and grain size distribution histograms for SCO, SCMO, 20SGCMO, and 50SGCMO compounds.

3.2 Electrical and Optical study

The temperature dependent electrical resistivity (ρ) was measured in the temperature range of 220 - 300 K. The variation of electrical resistivity ρ (Ω.m) against T (K) is plotted in Fig. 4 (a). As can be seen, the resistivity increases exponentially with decreasing temperature. Such kind of variation suggests that all compounds exhibit semiconducting-like nature. The

resistivity (ρ) at ~ 220 K for SCO and SCMO compounds is ~ 10^2 Ω.m. Further, adding Gd ions at Sm-site, resistivity order increases upto ~10^5 Ω.m which can be ascribed to the increased disorder due to the presence of varying size ions. The other reason may the increase in the tilt angles in the co-doped compounds which causes a deviation of the Cr-O-Cr bond angle from ideal 180° and the decrease in the conduction bandwidth. From the temperature dependent resistivity data, a ln (ρ) versus $1/T$ plot [Fig. 4(b)] was made using the Arrhenius equation: $\rho(T) = \rho_0 \exp(\frac{E_a}{k_B T})$. The activation energy (E_a) was estimated from the Arrhenius plots. The E_a values were found to be in the range of 0.193 - 0.225 eV (table 2). These values are consistent with those reported for others orthochromite materials [45 - 46]. Moreover, one can notice that E_a values of the present orthochromites are larger than those reported for CMR manganites. It indicates that hopping of e_g electrons is tougher in orthochromites than manganites [47 - 49]. The energy levels for Mn^{4+} ($3d^3$) and Cr^{3+} ($3d^3$) ions are different even with the same electronic state. The e_g electron can straightforwardly move between Mn^{4+}/Mn^{3+} through double-exchange (DE) interaction via O^{2-} ion, but in the Mn^{3+}/Cr^{3+} system it should meet an additional energy barrier because of the absence of DE interaction [49]. The larger activation energy value indicated the reduction of the hopping probability for e_g electrons.

To understand the electrical behavior of these compounds, the electrical resistivity data were fitted by Mott's variable-range hopping (VRH) model, the fitted data for all samples are shown in the inset of Fig. 4 (b). According to this model, the electrical resistivity versus temperature obeys the following expression [50]:

$$\rho(T) = \rho_0 \exp\left(\frac{T_0}{T}\right)^{1/4}, \text{ with } T_0 = \frac{18}{k_B N(E_F) l^3} \tag{1}$$

13

where ρ_0 is the residual resistivity, T_0 is the Mott characteristic temperature, k_B is the Boltzmann constant, $N(E_F)$ is the density of states near the Fermi level and 'l' is the localization length equal to lattice parameter. The hopping energy and mean hopping distance can be written at a given temperature, as $R_h = \left(\frac{3}{8}\right) l \left(\frac{T_0}{T}\right)^{\frac{1}{4}}$ and $W_h = \frac{1}{4} k_B T^{3/4} T_0^{1/4}$. The resistivity data fit very well with the Mott's VRH model for the entire temperature range of measurement, suggesting the conduction being governed by the disorder induced localization of charge carriers. The estimated values of $N(E_F)$, R_h and W_h at 300 K by using the Mott characteristic temperature (T_0) are summarized in table 2. The $N(E_F)$ slightly decreases with the Mn doping from $11.6{\times}10^{18}$ eV^{-1} cm^{-3} for SCO to $11.4{\times}10^{18}$ eV^{-1} cm^{-3} for SCMO whereas it significantly decreases with the substitution of Gd ions at Sm-site. On further enhancement of the doping concentration of Gd ions, $N(E_F)$ decreases from $8.78{\times}10^{18}$ eV^{-1} cm^{-3} for 10SGCMO to $6.83{\times}10^{18}$ eV^{-1} cm^{-3} for 50SGCMO compound. This is due to the increase in the resistivity with Mn and Gd substitution. The hopping distance and hopping energy increase with Mn doping from SCO to SCMO compound and it also increases with increase in Gd-content from 10 at. wt. % to 50 at. wt. %. These values are consistent with the earlier reports on other semiconductor manganites or orthochromites [51-52].
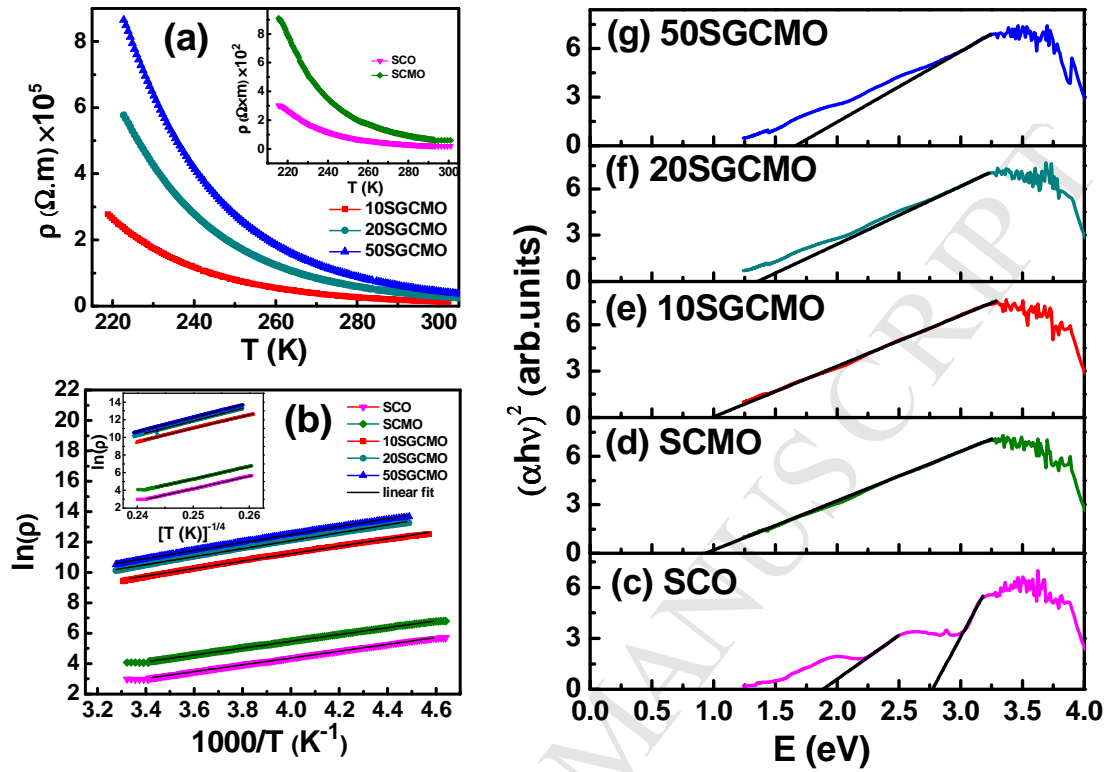
Figure 4. (a) Temperature variation of resistivity between 220-300 K, (b) Arrhenius plots, and (c-g) Tauc's plots of the SCO, SCMO, 10SGCMO, 20SGCMO and 50SGCMO samples.

The optical band gap of the all compounds was estimated with the help of Tauc's equation [53] given by,

$$\alpha h\nu = A(h\nu - E_g)^n \qquad (2)$$

here $h\nu$ being the energy of the incident photon, α stands for the absorption coefficient and A is a characteristic parameter. E_g denotes the optical band gap whereas $n = 1/2\,(2)$ for direct (indirect) transitions. The orthochromite materials shows directly allowed transitions [24, 54] . Using the above equation, the graph was plotted between $(\alpha h\nu)^2$ and $h\nu$ and shown in Fig. 4 (c-

15

g). The linear absorption-edge curve was fitted with a straight line the intersection of that with the horizontal axis provided the value of E_g, as summarized in table 2. In SCO compound, we observed two prominent peaks around 466 nm and 690 nm which are attributed to the transitions of O^{2p} - Cr^{3d} (t_{2g}) and Cr^{3d} (t_{2g}) - Cr^{3d} (e_g) due to octahedral crystal field splitting of d-orbitals. These transitions correspond to the band gap energy of 2.7 eV and 1.9 eV, respectively. These values are comparable to the previously reported results [55]. With 15% Mn substitution at Cr-site, the band gap energy decreases to 0.83 eV, due to a super-exchange interaction between the Cr^{3+} and Mn^{3+} electronic levels through O^{2-} ion. The Cr^{3+} and Mn^{3+} ions induce a spin disorder at oxygen ion which can reduce the broadening of oxygen p-orbitals and valance band edges of Cr^{3+} and Mn^{3+} ions, intimating a smaller band gap [24, 56]. Furthermore, as we substitute Gd^{3+} ions at Sm-site, the band gap energy increases up to 1.51 eV with increasing Gd concentration which can be attributed to the creation of mid gap states as reported in $Y_{1-x}Gd_xCrO_3$ nanoparticles [57]. The other reason for the increase in band-gap with Gd-doping is understood in terms of the decrease in R_{avg} and the corresponding increase in tilt angles. Finally, the optical band gap of SCO may be tuned by the co-doping of Mn and Gd ions at Cr-site and Sm-site, respectively, and signifies its potential application as a photocatalyst.

Table 2: Activation energy (E_a), Mott characteristic temperature (T_0), density of states at Fermi level $N(E_F)$, mean hopping distance (R_h), hopping energy (W_h) and optical band gap (E_g) of orthochromite samples.

Compound	SCO	SCMO	10SGCMO	20SGCMO	50SGCMO
E_a (eV)	0.193	0.194	0.210	0.225	0.227
$T_0 \times 10^6$ (K)	403	410	539	685	693
$N(E_F)$ $\times 10^{18}$ (eV^{-1}cm^{-3})	11.6	11.4	8.72	6.87	6.83
R_h (Å)	97.6	97.9	105	111.1	111.2

W_h (meV)	220	221	236	251	252
E_g (eV)	2.66	0.83	0.92	1.19	1.51

3.3 Magnetic properties

The SCO compound exhibits canted AFM below T_N (~192 K). In our previous study, we observed that T_N of SCO compound decreased to 168 K with 15% Mn doping [6]. This SCMO compound also exhibited magnetization reversal below T_N and change in spin structure from Γ_4 to Γ_2 at spin reorientation temperature (T_{SR}). In this article, we investigated the magnetic properties of all the co-doped compounds.

3.3.1 Magnetization reversal

Fig. 5 demonstrates the magnetization (M) versus temperature (T) plots for 10SGCMO, 20SGCMO and 50SGCMO compounds under the field-cooled (FC) and zero field-cooled (ZFC) modes at different applied magnetic field values. The AFM transition at T_N was calculated from the minimum of the first derivative of magnetization versus temperature plot. The observed values of T_N are ~162 K, ~157 K and ~150 K, respectively for these compounds. T_N follows a typical behavior with decreasing R_{avg} [26].

Fig. 5 (a) - (c) illustrates that ZFC and FC magnetization curves, measured under 1000 Oe field, are bifurcated below T_N. The M_{FC} magnetization value increases with decreasing temperature and attains a maximum value of magnetization (M_{Max}) with positive polarity at the peak temperature. After that, the magnetization starts decreasing monotonously and crosses zero magnetization ($M = 0$) at the compensation temperature (T_{comp1}). Finally, it approaches a minimum value M_{Min} at T_{SR} (defined as spin reorientation transition). The negative value of magnetization indicates the opposite direction of the net magnetic moment with respect to the

applied magnetic field. The moments of Sm^{3+}, Gd^{3+} and Mn^{3+} ions get aligned antiparallel to weak ferromagnetic (WFM) components of the Cr^{3+} spins causing magnetization reversal phenomenon in these compounds [37]. Further below T_{SR}, the magnetization again crosses zero at temperature T_{comp2} and becomes positive. On the other hand, magnetization remains positive below T_{comp1} in case of ZFC mode. The values of T_{comp1}, T_{comp2} and T_{SR} are listed in table 3. The T_{comp1} decreased with increasing doping concentration of Gd ions (excluding 20SGCMO compound) following the trend of T_N. The magnitude of magnetization reversal is usually measured from the ratio of M_{Min} and M_{Max}. Here, one can notice that the ratio M_{Min}/M_{Max} decreased with increasing doping concentration of Gd ions excluding 20SGCMO compound (table 3). The maximum value of M_{Min}/M_{Max} was found to be -6.2 for 20SGCMO compound, that is lower than that for the SCMO compound. Therefore, these compounds clearly demonstrate the effect of co-doping (Gd & Mn magnetic ions) in tailoring the magnetic behavior of $SmCrO_3$ compound. Such tuning of magnetization with co-doping may be suitable for thermomagnetic devices utilizing the flipping magnetization with temperature.

At higher applied field values (*i.e.* 2500 Oe), similar behavior was observed in the magnetization curves. The magnetic irreversibility (*i.e.* bifurcation between the ZFC and FC curves below T_N) decreases in comparison to low field values for 10SGCMO and 20SGCMO compounds [Fig. 5(d) - (e)]. On the contrary, magnetization reversal completely disappeared in the case of 50SGCMO compound at 2500 Oe magnetic field [Fig. 5 (f)]. Furthermore, the magnetization becomes positive in the entire temperature range of measurement under an applied field of 5000 Oe [Fig. 5(g) - (i)] in both ZFC and FC modes for all the studied compounds because of the rotation of the moments of Mn^{3+} and Sm^{3+}/Gd^{3+} ions along the field as the applied field dominates the internal field.

18

Table 3: The parameters are M_{Min}/M_{Max}, T_{comp1}, T_{comp2}, T_{SR}, M_{Cr}, H_I and θ for co-doped SCO orthochromites

	SCMO [ref[6]]	10SGCMO		20SGCMO		50SGCMO
H (Oe)	1000	1000	2500	1000	2500	1000
M_{Min}/M_{Max}	−12.09	−6.43	−1.49	−6.82	−0.56	−0.38
T_{comp1} (K)	103	93	75	97	65	65
T_{comp2} (K)	8	11	21	8	19	23
T_{SR} (K)	17	22	27	17	32	30
M_{Cr} (emu/g)	0.865	0.703	0.813	0.879	0.994	0.668
H_I (Oe)	−1104	−1068	−2546	−1084	-2581	−1086
θ (K)	−86	−34	−81	−60	−163	−163

Further, the FC magnetization curves were fitted (from peak temperature to T_{SR}) using the following equation [3];

$$M = M_{Cr} + \frac{C(H_I + H)}{T - \theta} \tag{3}$$

Where M_{Cr} is the weak FM component of canted Cr^{3+} ions, C is the Curie constant, H_I is the internal field, H is the applied field and θ is the Weiss temperature. The fitting is shown by solid line in Fig. 5 (a - e). The obtained fitting parameters are listed in table 3. The values of internal field (H_I) for all co-doping compounds are negative, confirming the assumption that it isopposite to the applied field because of its value being larger than the applied magnetic field. This allows the magnetization of ions to get aligned antiparallel to that of Cr^{3+} ions when the applied field is smaller. Furthermore, the magnitude of H_I decreases with increase of applied field for all the co-doped compounds, as shown in the table 3.

19
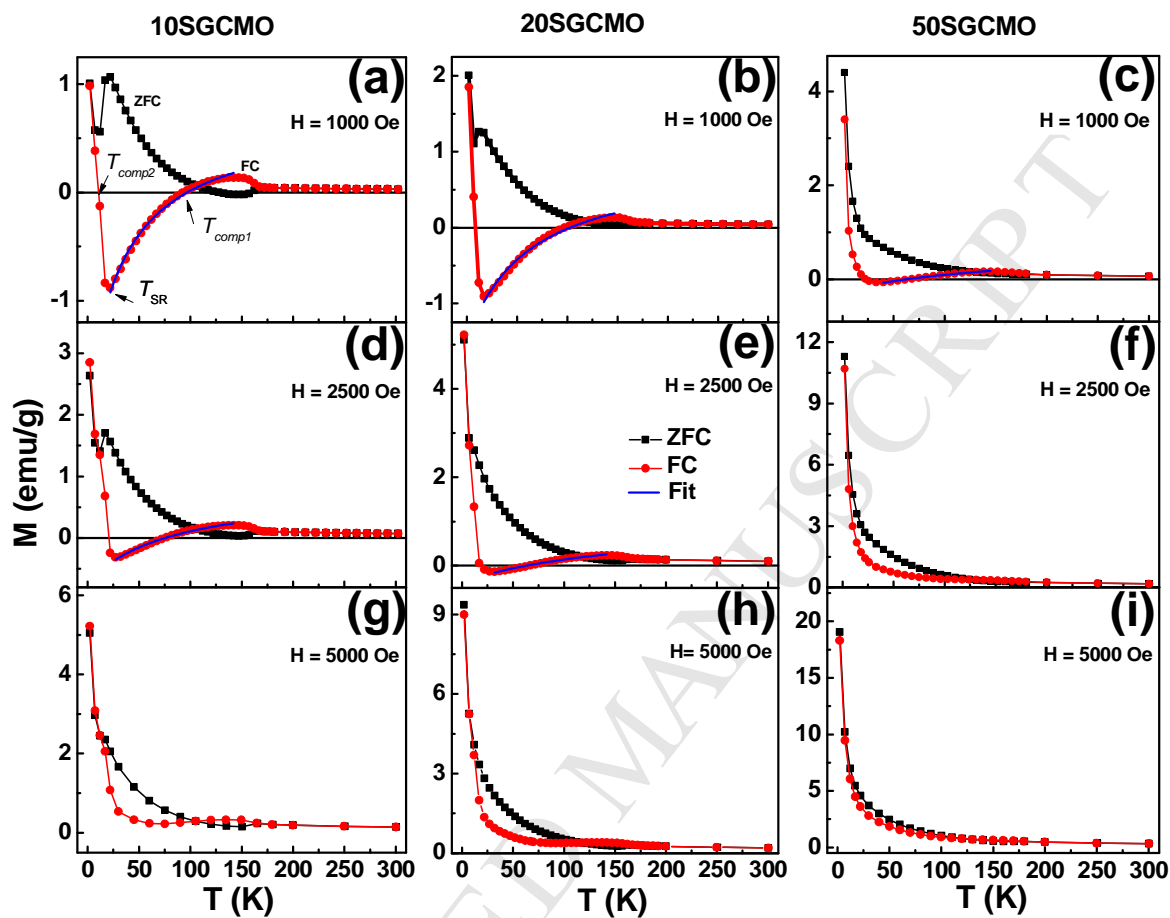
10SGCMO

20SGCMO

50SGCMO

Figure 5: Temperature dependent magnetization curves; (a, d, g) for 10SGCMO, (b, e, h) for 20SGCMO, and (c, f, i) for 50SGCMO measured under different applied field. The solid blue line shows the Curie - Weiss fit of the FC data.

3.3.2 M-H loops

In order to better understand about the magnetic behavior of these compounds, we measured isothermal magnetization (M) loops as a function of applied field (H) (in the range $\pm$ 90 kOe) at different temperatures. Fig. 6 (a - c) displays the typical M - H loops at selected

20

temperatures of 2, 20 and 80 K for 10SGCMO, 20SGCMO and 50SGCMO compounds. For all these compounds, loops are well symmetrically closed without any saturation. A weak magnetic hysteresis is observed at lower field as shown in the insets of Fig. 6 (a - c). Such behavior is reminiscent of the coexistence of high field AFM and low field weak ferromagnetic (FM) components. The antisymmetric DM interaction is responsible for the weak FM component. Thus, the present *M-H* curves evolution can be represented as $M(H) = \chi_{AFM}H + M_S$. Here $\chi_{AFM}H$ is the AFM contribution and M_s is the saturation magnetization of the weak FM phase. The saturation magnetization of weak FM component (M_s) can be calculated by subtracting the high field linear AFM contribution from the total magnetization. Fig. 6 (d) shows coercive field (H_c) and M_s plotted against doping concentration of Gd ions at 2 K and 20 K. The M_S values increased with increasing doping concentration of Gd ions at both the temperatures [Fig. 6 (d) lower panel]. The H_c values increased at 2 K (near the magnetic ordering temperature of Gd^{3+} ions) and decreased at 20 K (near T_{SR}) with increasing doping concentration of Gd ions [Fig. 6 (d) upper panel].
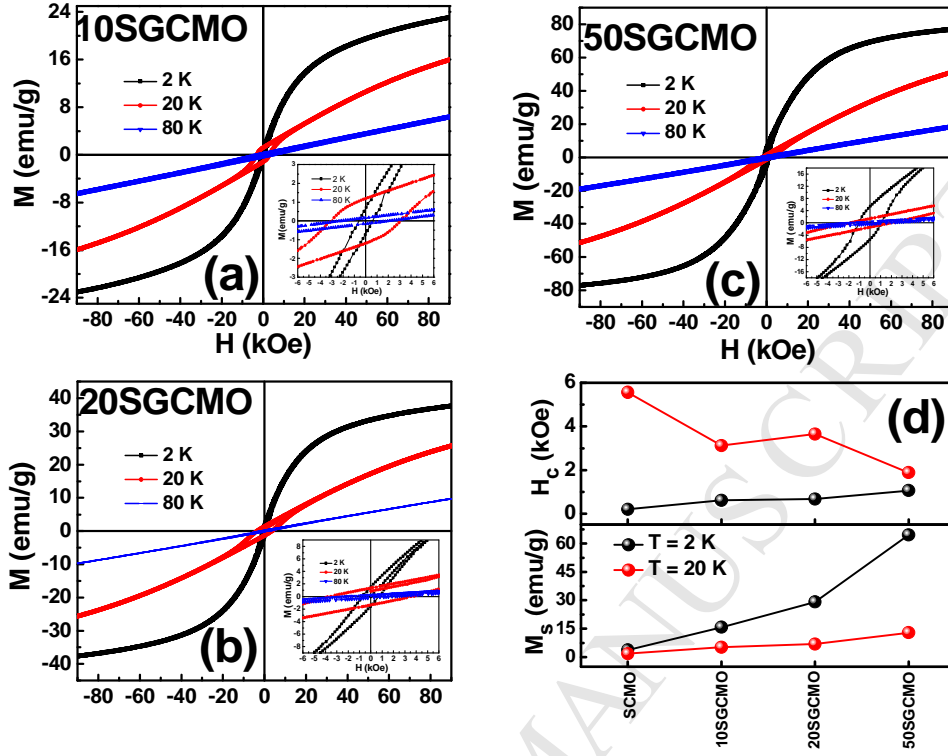
Figure 6: *M-H* curves measured at 2K,20K and 80K; (a) 10SGCMO, (b) 20SGCMO and (c) 50SGCMO (insets show zoomed views of *M-H* curves at lower fields). (d) coercive field and saturation magnetization against doping concentration of Gd ions at 2 K and 20 K.

3.4 Magnetocaloric effect

To study the impact of co-doping on the MCE, we measured *M-H* curves in first quadrant with appliedfield up to 90 kOe, at different temperature for the 10SGCMO, 20SGCMO and 50SGCMO compounds. The plots are shown in Fig. 7 (a-c).The evaluated MCE behavior of the compounds can be extracted from the isothermal magnetization curves and magnetic entropy change defined as [58]

$$\Delta S(T)_{\Delta H} = \int_{H_I}^{H_F} \left(\frac{\partial M(T,H)}{\partial T}\right)_H dH \tag{4}$$

Numerical integration of the above Eq. by trapezoidal rule results [59]

$$\Delta S(T_{av})_{\Delta H} = \frac{\delta H}{2\,\delta T}\left(\delta M_1 + 2\sum_{i=2}^{n-1}\delta M_i + \delta M_n\right) \qquad (5)$$

where average temperature T_{av} [$= (T_j + T_{j+1})/2$] is taken from the two magnetization isotherms measured at T_j and T_{j+1} temperatures in a magnetic field changing by $\Delta H = H_F - H_I$ at a constant step of δH, while $\delta T = T_{j+1} - T_j$ is the temperature difference between the two isotherms, n is the number of points measured for each of the two isotherms with the magnetic field changing from $H_1 = H_I$ to $H_n = H_F$ at $\delta H = \Delta H/(n-1)$. Further, $\delta M_i = [M(T_{j+1})_i - M(T_j)_i]$ is the difference in the magnetization at T_{j+1} and T_j for each magnetic-field step from 1 to n. Fig. 7 (d) shows the temperature dependent $-\Delta S$ at 50 kOe magnetic field and $-\Delta S_{Max}$ under other field values are summarized in table 4. The value of $-\Delta S$ increases sharply with decreasing temperature and reaches a maximum value of 3.25, 6.23 and 14.01 J kg^{-1} K^{-1} at 4.5 K, respectively for 10SGCMO, 20SGCMO and 50SGCMO compounds on a 0 - 50 kOe field variation. One notices here that the MCE got enhanced with increasing Gd doping concentration. On comparing the $-\Delta S$ values of the present study with that for the SCMO compound reported by Kumar *et al.* [6], we observed that the compounds 10SGCMO, 20SGCMO and 50SGCMO yielded almost two times, six times and fourteen times higher than SCMO compound. As compared to the reported values of $-\Delta S$ in the literature for some orthochromites and orthoferrites are 13.08 J/kg K (at 5 K),19.02 J/kg K (at 4.5 K) under applied field of 70 kOe and 11.3 J/kg K (at 5 K) under applied field of 45 kOe for the $DyCr_{0.7}Fe_{0.3}O_3$ [60], $HoFeO_3$ (single crystal) [61] and $DyCr_{0.5}Fe_{0.5}O_3$ [44], respectively. The 50SGCMO of the present study yielded 14.10 J/kg K value under 50 kOe applied field, which is much higher than that reported for the undoped SCO compound [36] and comparable to the above-mentioned reported compounds exhibiting significant magnetocaloric effect. Several factors contributed to the enhancement of the MCE of the present co-doped

compounds. Firstly, these compounds exhibit higher magnetization and lower coercive field therefore less energy would be lost in thermal process resulting in the increase of $-\Delta S$ values. Secondly, $-\Delta S$ values not only depend on the magnetic moments but also on (dM/dT) according to Eq. (4). Thirdly, the Gd^{3+}- Gd^{3+} magnetic interactions near the magnetic ordering temperature of Gd^{3+} (at 2.3 K) will also contribute in enhancing $-\Delta S$ values of the co-doped compounds. The increase in tilt angles in the co-doped compounds may result in the increase of magnetic entropy and its contribution to the enhancement of the magnetic entropy change. We further calculated another parameter for the estimation of MCE of the compounds. It is the relative cooling power (RCP) obtained from the integration method:

$$RCP = \int_{T_1}^{T_2} \Delta S(T)_{\Delta H} \, dT \tag{6}$$

where T_1 and T_2 are the low and high temperature limits in the refrigeration cycle ($T_1 = 4.5$ K and $T_2 = 25$ K in the present study) at different magnetic field values. The RCP values of 10SGCMO, 20SGCMO and 50SGCMO compounds were 33.11, 62.69, and 152.31 J/kg, respectively (table 4) at 50 kOe. The RCP values also increased with increasing Gd substitution. Based on the calculations of two parameters for MCE viz. $-\Delta S$ and RCP, we conclude that co-doping is a powerful methodology for enhancing the magnetocaloric properties of orthochromites at low temperatures and the studied compounds could be potential candidates as refrigerant at low temperatures.

Table 4: Magnetic entropy change and relative cooling power at various applied magnetic fields of co-doped SCO compounds

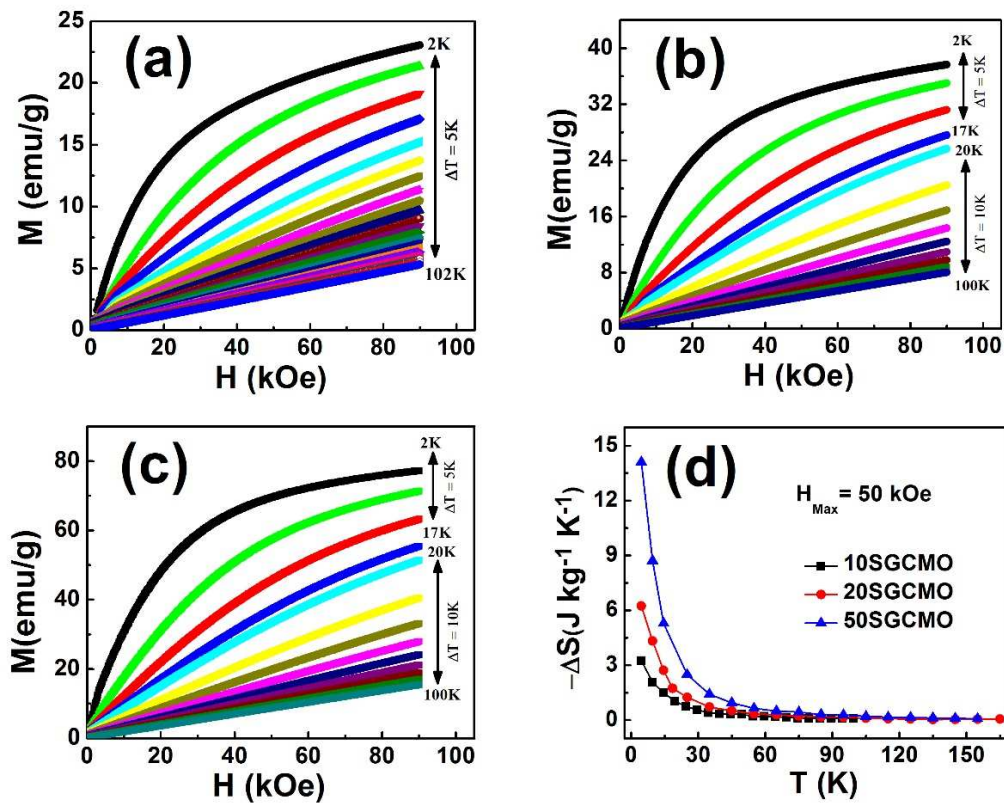| H_{Max} (kOe)	10SGCMO		20SGCMO		50SGCMO	
	$-\Delta S_{Max}$ (J kg^{-1} K^{-1})	RCP (J kg^{-1})	$-\Delta S_{Max}$ (J kg^{-1} K^{-1})	RCP (J kg^{-1})	$-\Delta S_{Max}$ (J kg^{-1} K^{-1})	RCP (J kg^{-1})
10	0.39	2.19	0.75	4.41	1.59	9.39
30	1.99	15.71	3.79	30.42	8.25	62.59
50	3.25	33.11	6.23	62.69	14.10	152.31
70	4.16	50.22	7.93	94.05	18.11	201.24
90	4.91	66.40	9.13	122.27	20.84	262.51

Figure 7: (a-c) Isothermal M-H curve (in first quadrant) at selected temperatures, (d) temperature dependent magnetic entropy change ($-\Delta S$) under 50 kOe applied field for 10SGCMO, 20SGCMO, and 50SGCMO compounds.

4   Conclusions

For the first time; structural, electrical, optical and magnetic properties of Gd and Mn ions co-doped $SmCrO_3$ compound have been carried out. The lattice volume decreased whereas the orthorhombic distortion increased in the co-doped samples. The average grain size increased from 0.73 μm (SCO) to 2.19 μm (50SGCMO). The activation energy calculated from the electrical resistivity data using the Arrhenius equation got enhanced in the co-doped samples. Further, the Mott's variable range hopping model was used to explain the electrical resistivity behavior and the hopping energy and mean hopping distance were found to increase whereas the density of states decreased in the co-doped compounds. The optical bandgap reduced with Mn doping from 2.66 eV for SCO to 0.83 eV for SCMO compound and then increased monotonously upto 1.51 eV for 50SGCMO compound. The paramagnetic-antiferromagnetic transition shifted to lower temperatures with increasing co-doping level. The overall magnetization increased with co-doping. Two compensation temperatures were identified in the co-doped compounds. While the higher temperature compensation temperature decreased, the lower temperature compensation temperature increased with co-doping. The observed magnetization reversal was explained based on the existing model. The low temperature magnetocaloric effect got enhanced with increasing co-doping content and its values are significantly larger than the undoped SCO compound. These studies prove the usefulness of the present co-doped compounds as photocatalyst and low temperature refrigerant materials.

References:

[1]   Hill N A 2000 Why are there so few magnetic ferroelectrics? *J. Phy.Chem.B* **104 (29)** 6694–709

[2]   Kimura T, Goto T, Shintani H, Ishizaka K, Arima T and Tokura Y 2003 Magnetic control of ferroelectric polarization *Nature* **426** 55–8

[3]   Cooke A H, Martin D M and Wells M R 1974 Magnetic interactions in gadolinium orthochromite, GdCrO$_3$ *J. Phys. C Solid State Phys.***7** 3133–44

[4]   Cao Y, Cao S, Ren W, Feng Z, Yuan S, Kang B, Lu B and Zhang J 2014 Magnetization switching of rare earth orthochromite CeCrO$_3$ *Appl. Phys. Lett.***104** 1–5

[5]   Yoshii K 2012 Magnetization reversal in TmCrO$_3$ *Mater. Res. Bull.***47** 3243–8

[6]   Kumar S, Coondoo I, Vasundhara M, Patra A K, Kholkin A L and Panwar N 2017 Magnetization reversal behavior and magnetocaloric effect in SmCr$_{0.85}$Mn$_{0.15}$O$_3$ chromites

27

J. Appl. Phys. **121** 43907

[7]   Kumar S, Coondoo I, Rao A, Lu B-H, Kuo Y-K, Kholkin A L and Panwar N 2017 Impact of low level praseodymium substitution on the magnetic properties of $YCrO_3$ orthochromites *Phys. B Condens. Matter* **510** 104–8

[8]   Gupta P and Poddar P 2015 Temperature and Magnetic Field-Assisted Switching of Magnetization and Observation of Exchange Bias in $YbCrO_3$ Nanocrystals *Inorg. Chem.* **54** 9509–16

[9]   Kumar S, Coondoo I, Vasundhara M, Puli V S and Panwar N 2017 Observation of magnetization reversal and magnetocaloric effect in manganese modified $EuCrO_3$ orthochromites *Phys. B Condens. Matter* **519** 69–75

[10]   Yoshii K 2011 Positive exchange bias from magnetization reversal in $La_{1-x}Pr_xCrO_3$ (x $\square$ 0.7–0.85) *Appl. Phys. Lett.* **99** 142501

[11]   Wang L, Rao G H, Zhang X, Zhang L L, Wang S W and Yao Q R 2016 Reversals of magnetization and exchange-bias in perovskite chromite $TmCrO_3$ *Ceram. Int.* **42** 10171–4

[12]   Stanciu C D, Tsukamoto A, Kimel A V, Hansteen F, Kirilyuk A, Itoh A and Rasing T 2007 Subpicosecond magnetization reversal across ferrimagnetic compensation points *Phys. Rev. Lett.* **99** 217204

[13]   Graves C E, Reid A H, Wang T, Wu B, de Jong S, Vahaplar K, Radu I, Bernstein D P, Messerschmidt M, Müller L, Coffee R, Bionta M, Epp S W, Hartmann R, Kimmel N, Hauser G, Hartmann A, Holl P, Gorke H, Mentink J H, Tsukamoto A, Fognini A, Turner J J, Schlotter W F, Rolles D, Soltau H, Strüder L, Acremann Y, Kimel A V, Kirilyuk A,

Rasing T, Stöhr J, Scherz A O and Dürr H A 2013 Nanoscale spin reversal by non-local angular momentum transfer following ultrafast laser excitation in ferrimagnetic GdFeCo. *Nat. Mater.* **12** 293–8

[14] Kumar A and Yusuf S M 2015 The phenomenon of negative magnetization and its implications *Phys. Rep.* **556** 1–34

[15] Bandiera S and Dieny B 2015 Thermally assisted MRAM *Handb. Spintron.* **165218** 1065–100

[16] Kumar S, Coondoo I, Vasundhara M, Kumar S, Kholkin A L and Panwar N 2017 Structural, magnetic , magnetocaloric and specific heat investigations on Mn doped PrCrO 3 orthochromites *J. Phys. Condens. Matter* **29** 195802

[17] Dzyaloshinsky I 1958 A thermodynamic theory of "weak" ferromagnetism of antiferromagnetics *J. Phys. Chem. Solids* **4** 241–55

[18] Moriya T 1960 Anisotropic Superexchange Interaction and Weak Ferromagnetism *Phys. Rev.* **120** 91

[19] Sfeir J 2003 LaCrO$_3$-based anodes: Stability considerations *J. Power Sources* **118** 276–85

[20] Zwinkels M F M, Haussner O, Menon P G and Järås S G 1999 Preparation and Characterization of LaCrO$_3$ and Cr$_2$O$_3$ Methane Combustion Catalysts Supported on LaAl$_{11}$O$_{18}$- and Al$_2$O$_3$-Coated Monoliths *Catal. Today* **47** 73–82

[21] Soltani N, Hosseini S M and Kompany A 2009 Nanoscale ab-initio calculations of optical and electronic properties of LaCrO$_3$ in cubic and rhombohedral phases *Phys. B Condens. Matter* **404** 4007–14

[22]   Siemons M and Simon U 2007 High throughput screening of the propylene and ethanol sensing properties of rare-earth orthoferrites and orthochromites *Sensors Actuators, B Chem.* **126** 181–6

[23]   Gupta P and Poddar P 2015 RSC Advances Using Raman and dielectric spectroscopy to elucidate the spin phonon and magnetoelectric *RSC Adv.* **5** 10094–101

[24]   Kotnana G and Jammalamadaka S N 2015 Band gap tuning and orbital mediated electron – phonon coupling *J. Appl. Phys.* **118** 1–7

[25]   Nichols J, Yuk S F, Sohn C, Jeen H, Freeland J W, Cooper V R and Lee H N 2017 Electronic and magnetic properties of epitaxial $SrRhO_3$ films *Phys. Rev. B* **95** 245121

[26]   Yin S, Seehra M S, Guild C J, Suib S L, Poudel N, Lorenz B and Jain M 2017 Magnetic and magnetocaloric properties of $HoCrO_3$ tuned by selective rare-earth doping *Phys. Rev. B* **95** 184421

[27]   Sharma M K and Mukherjee K 2017 Magnetic and universal magnetocaloric behavior of rare-earth substituted $DyFe_{0.5}Cr_{0.5}O_3$ *J. Magn. Magn. Mater.* **444** 178–83

[28]   Yin S, Sharma V, McDannald A, Reboredo F A and Jain M 2016 Magnetic and magnetocaloric properties of iron substituted holmium chromite and dysprosium chromite *RSC Adv.* **6** 9475–83

[29]   Yin L H, Yang J, Kan X C, Song W H, Dai J M and Sun Y P 2015 Giant magnetocaloric effect and temperature induced magnetization jump in $GdCrO_3$ single crystal *J. Appl. Phys.* **117** 0–8

[30]   Mcdannald A, Kuna L and Jain M 2013 Magnetic and magnetocaloric properties of bulk

dysprosium chromite *J. Appl. Phys.* **114** 113904

[31] Gupta P, Bhargava R and Poddar P 2015 Colossal increase in negative magnetization, exchange bias and coercivity in samarium chromite due to a strong coupling between Sm^{3+}–Cr^{3+} spins sublattices *J. Phys. D. Appl. Phys.* **48** 25004

[32] Dash B B and Ravi S 2016 Sign reversal of magnetization in Mn substituted $SmCrO_3$ *J. Magn. Magn. Mater.* **405** 209–13

[33] Wu Y, Xu J and Xia Z 2016 Temperature-Induced Magnetization Reversal in the Mn^{3+}-Doped $SmCrO_3$ *J. Low Temp. Phys.* **183** 14–22

[34] Huang S, Zerihun G, Tian Z, Yuan S, Gong G, Yin C and Wang L 2014 Magnetic exchange bias and high-temperature giant dielectric response in $SmCrO_3$ ceramics *Ceram. Int.* **40** 13937–43

[35] El Amrani M, Zaghrioui M, Ta Phuoc V, Gervais F and Massa N E 2014 Local symmetry breaking and spin-phonon coupling in $SmCrO_3$ orthochromite *J. Magn. Magn. Mater.* **361** 1–6

[36] Gupta P and Poddar P 2016 Study of magnetic and thermal properties of $SmCrO_3$ polycrystallites *RSC Adv.* **6** 82014–23

[37] Panwar N,Joby P J, Kumar S, Coondoo I, VasundharaM., Kumar N, Palai R, Singhal R and KatiyarS R 2017 Observation of Magnetization reversal behavior in $Sm_{0.9}Gd_{0.1}Cr_{0.85}Mn_{0.15}O_3$ orthochromites *AIP Adavance* **8** 55818

[38] Shannon R D 1976 Revised effective ionic radii and systematic studies of interatomic distances in halides and chalcogenides *Acta Crystallogr. Sect. A* **32** 751–67

[39]   Ghosh   A, Dey K, Chakraborty M, Majumdar S and Giri S 2014 Polar octahedral rotations, cation displacement and ferroelectricity in multiferroic SmCrO$_3$ *Euro Phys. Lett.* **107** 47012

[40]   Weber M C, Kreisel J, Thomas P A, Newton M, Sardar K and Walton R I 2012 Phonon Raman scattering of RCrO$_3$ perovskites (R=Y, La, Pr, Sm, Gd, Dy, Ho, Yb, Lu) *Phys. Rev. B* **85** 054303

[41]   Zhao Y, Weidner D J, Parise J B and Cox D E 1993 Thermal expansion and structural distortion of perovskite - data for NaMgF$_3$ perovskite. Part I *Phys. Earth Planet. Inter.* **76** 1–16

[42]   Glazer A M 1972 The classification of tilted octahedra in perovskites *Acta Crystallogr. Sect. B Struct. Crystallogr. Cryst. Chem.* **28** 3384–92

[43]   Iliev M N, Lee H-G, Popov V N, Sun Y Y, Thomsen C, Meng R L and Chu C W 1998 Raman spectroscopy of orthorhombic perovskitelike YMnO$_3$ and LaMnO$_3$ *Phys. Rev. B* **57** 2872–7

[44]   Yin L H, Yang J, Zhang R R, Dai J M, Song W H and Sun Y P 2014 Multiferroicity and magnetoelectric coupling enhanced large magnetocaloric in DyFe$_{0.5}$Cr$_{0.5}$O$_3$ *Appl. Phys. Lett.* **104** 32904

[45]   Selvadurai A P B, Pazhanivelu V, Jagadeeshwaran C, Murugaraj R, Panneer Muthuselvam I, Chou F C, Md Gazzali P M and Chandrasekaran G 2016 Structural, magnetic and electrical analysis of La$_{1-x}$Nd$_x$CrO$_3$ (0.00≤x ≤ 0.15): synthesised by sol–gel citrate combustion method *J. Sol-Gel Sci. Technol.* **80** 827–39

[46] Nithya V D, Jacob Immanuel R, Senthilkumar S T, Sanjeeviraja C, Perelshtein I, Zitoun D and Kalai Selvan R 2012 Studies on the structural, electrical and magnetic properties of $LaCrO_3$, $LaCr_{0.5}Cu_{0.5}O_3$ and $LaCr_{0.5}Fe_{0.5}O_3$ by sol-gel method *Mater. Res. Bull.* **47** 1861–8

[47] Ziese M and Srinitiwarawong C 1998 Polaronic effects on the resistivity of manganite thin films *Phys. Rev. B* **58** 11519

[48] Liu J M, Huang Q, Li J, Ong C K, Wu Z C, Liu Z G and Du Y W 2000 Effect of oxygen nonstoichiometry on electrotransport and low-field magnetotransport property of polycrystalline $La_{0.5}Sr_{0.5}MnO_3$ thin films *Phys. Rev. B* **62** 8976

[49] Yang L, Duanmu Q, Hao L, Zhang Z, Wang X, Wei Y and Zhu H 2013 Ferrimagnetism and possible double perovskite structure in half Cr-doped $YMn_{0.5}Cr_{0.5}O_3$ *J. Alloys Compd.* **570** 41–5

[50] Mott N F 1975 Conduction in non-crystalline systems *Philos. Mag.* **32** 159–71

[51] Khan W, Naqvi A H, Gupta M, Husain S and Kumar R 2011 Small polaron hopping conduction mechanism in Fe doped $LaMnO_3$ *J. Chem. Phys.* **135** 1–7

[52] Modi A and Gaur N K 2015 Structural, electrical and magnetic phase evolution of Cr substituted $GdMn_{1-x}Cr_xO3(0 \leq x \leq 0.2)$ manganites *J. Alloys Compd.* **644** 575–81

[53] Fridman 1966 Optical Properties and Electronic Structure of Amorphous Germanium *Phys. Status Solidi* **15** 627–37

[54] Saha S, Chanda S, Dutta A and Sinha T P 2014 Dielectric relaxation and phonon modes of $NdCrO_3$ nanostructure *J. Sol-Gel Sci. Technol.* **69** 553–63

[55] Nashim A and Parida K M 2013 Novel $Sm_2Ti_2O_7$ /$SmCrO_3$ heterojunction based

compositephotocatalyst for degradation of Rhodamine 6G dye Chem. Eng. J. **215–216** 608–15

[56] Arima T, Tokura Y and Torrance J B 1993 Variation of optical gaps in perovskite-type 3d transition-metal oxides *Phys. Rev. B* **48** 17006–9

[57] Sinha R, Basu S and Meikap A K 2018 The investigation of the electrical transport properties of Gd doped $YCrO_3$ nanoparticles *Mater. Res. Bull.* **97** 578–87

[58] Tishin A M, SpichkinY I 2003 *The Magnetocaloric Effect and its Applications* (CRC Press: Taylor & Francis Group)

[59] Pecharsky V K and Gschneidner K a. 1999 Magnetocaloric effect from indirect measurements: Magnetization and heat capacity *J. Appl. Phys.* **86** 565

[60] Yin S, Sharma V, Mcdannald A, Reboredo A and Jain M 2016 Magnetic and magnetocaloric properties of iron substituted holmium chromite and dysprosium chromite *RSC Adv.* **6** 9475–83

61] Shao M, Cao S, Wang Y, Yuan S, Kang B and Zhang J 2012 Large magnetocaloric effect in $HoFeO_3$ single crystal *Solid State Commun.* **152** 947–50

Highlights (for review)

- Effect of Gd and Mn co-substitution in $SmCrO_3$ investigated for the first time
- Three orders of magnitude increase in electrical resistivity with co-doping
- Optical bandgap tailoring with co-doping
- Two magnetization reversal temperatures in co-doped compounds
- Two orders of magnitude surge in magnetocaloric properties with co-doping